DOI: 10.1478/AAPP.96S1A6

AAPP | Atti della Accademia Peloritana dei Pericolanti
Classe di Scienze Fisiche, Matematiche e Naturali
ISSN 1825-1242

Vol. 96, No. S1, A6 (2018)

INTERRUPTION OF THE STRAIN RATE SENSITIVITY OF METALS AT THE NECKING ONSET

GIUSEPPE MIRONE,[a*] DOMENICO CORALLO[a] AND RAFFAELE BARBAGALLO[a]

ABSTRACT. In this work, the interaction between the necking onset and the strain rate sensitivity in tensile tests by Split Hopkinson Tensile Bar (SHTB) is investigated. Results from experiments on a FE360 mild steel done by the authors and experimental data available in the literature for a Remco iron are discussed here to investigate the phenomenon. In both cases, images from high speed camera allowed to obtain the true curve of the material, calculating the actual necking section area from the optical measurement of the diameter. Moreover, the implications of such phenomenon on the characterization of materials using an SHTB is discussed.

Notation

Symbol	Description
σ_{Eq}	von Mises equivalent stress
σ_{True}	True stress, load/current cross section ratio, mean axial stress
ε_{True}	True strain, logarithm of (undeformed cross section / current cross section)
T^*	Temperature parameter of Johnson-Cook hardening
MLR	Approximate function for transforming the experimental true stress into the von Mises stress
L_0	Initial undeformed gage length of the specimen
L	Current gage length of the specimen
A_0	Initial undeformed cross section area of the specimen
A	Current necked area of the specimen
F	Current tensile load
ε_N	True strain at the necking onset
$R(\dot{\varepsilon}_{Eq})$	General expression of the dynamic stress amplification
$S(T)$	General expression of the thermal softening
RFast	R function from faster exp. test
RSlow	R function from slower exp. test
RFlat	R function incorporating arbitrary freezing effect
ε_{Eng}	Engineering strain, current elongation/initial gage length
t_R	Rise time of the incident wave

This paper is dedicated to the memory of Prof. Gaetano Giaquinta (1945–2016)

1. Introduction

The necking in high strain rate tests is still an interesting and not fully understood phenomenon. Rusinek *et al.* (2005) studied the correlation betweenthe critical impact velocity and multiple necking withthe energy storage capability of specimen, Besnard *et al.* (2012) obtained accuratenecking measurementsby means of stereocorrelation, while Sato *et al.* (2015) obtained detailed distributions of necking-affected strains and fracture surfacesusing Digital Image Correlation (DIC).

Moreover, as forthe quasistatic case, in order to accurately characterize the materialsat high strain rate it is necessary to determinethe equivalent stress σ_{Eq} rather thanthe true stress, which can beobtainedvia fast camera acquisition by means of the optical calculation of the actual diameter.

The most known postnecking correction is due to Bridgman (1952), although the reverse engineering approach based on finite elements and on the simple engineering data is also diffused in the literature: according to this approach, the von Mises curve in input to Finite Element (FE) simulations is repeatedly varied by optimization algorithm until the engineering curve predicted by FE becomes similar enough to the experimental results.

A faster procedure for transforming the σ_{True} into an estimation of σ_{Eq} by a simple corrective function, called MLR, was introduced with regard to the quasistatic necking by Mirone (2004).

The material-independent MLR polynomial, depending on the post-necking strain, expresses the ratio $\sigma_{Eq}/\sigma_{True}$ for many metals including various kinds of steel, aluminium alloys and copper alloys; then, the MLR polynomial multiplied by the experimental true curve delivers the von Mises curve with an approximation within 5%, without any need for special measurements nor any other time-consuming procedure. Mirone (2013) checked the suitability of such procedure for also correcting the dynamic true curves with reference to the Remco iron, tested by Noble *et al.* (1999), who also calibrated the corresponding Johnson-Cook formulation.

In this work, the interactions between necking and strain rate are investigated through FE simulations based on the experiments by Noble *et al.* (1999) on a Remco iron and on other fast camera-assisted experiments performed by the authors on a FEN steel. According to the methodology used by Sato *et al.* (2015), Noble *et al.* (1999), Peirs *et al.* (2011), Mirone *et al.* (2016) and Mirone *et al.* (2017), σ_{True}, ε_{True} and $\dot{\varepsilon}_{True}$ are calculated by experiments also in the postnecking range and a material model of the dynamic hardening is developed and checked using FE simulations.

Once the good agreement between the experiments and the simulations is checked, modifications of the hardening functions are introduced for further investigating the interactions between necking and strain rate effect. The results shown a previously unknown phenomenon, just recently introduced by Mirone *et al.* (2017): The necking freezes the amplification caused by the strain rate on the σ_{Eq} (ratio of load to current area) and, in turn, on σ_{Eq} too. Given that only the true curve can be directly obtained from experiments without special hypothesis nor modelling assumption, it follows that the freezing phenomenon limits the strain rates really affecting the dynamic characterization to a fraction of those actually occurring on the specimens.

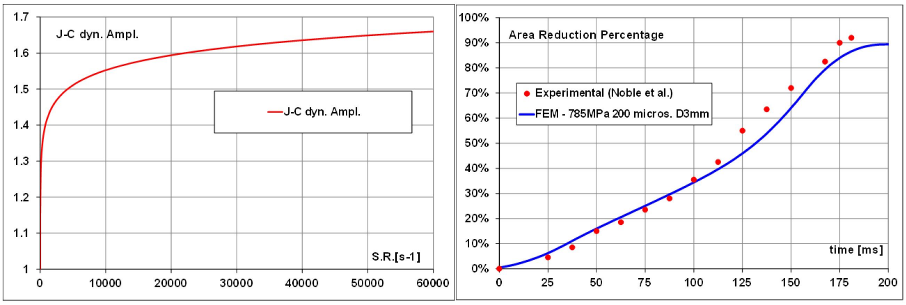

FIGURE 1. Experimental validation of the material parameters for the Remco Iron (Mirone 2013).

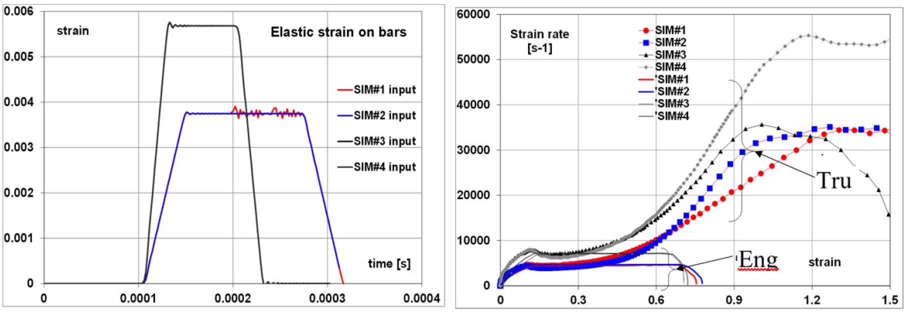

FIGURE 2. Incident waves and true strain rates simulated on the Remco Iron

2. SHTB experiments and modeling of a Remco iron from literature: FE validation and necking analysis

Noble *et al.* (1999) illustrated the results of experiments by SHTB on a low carbon steel identified as Remco iron and simulated the tests by finite elements; the Johnson-Cook model of dynamic hardening was calibrated as in Equation (1), where the dynamic amplification is the second bracket and it is shown in the left side of Figure 1,

$$\sigma_{Eq} = \left(175 + 380 \cdot \varepsilon_{True}^{0.32})\right) \left(1 + 0.06 \cdot \ln(\dot{\varepsilon}_{True})\right) \left(1 - T^{*0.55}\right). \qquad (1)$$

The above material model was used to simulate the SHTB Noble's tests discussed by (Mirone 2013), where it is possible to find further details. The simulations correctly reproduced the area reduction evaluated by Noble *et al.* (1999) through fast camera acquisition, as shown on the right side of Figure 1.

In fact, the left side of Figure 1 reports the trend of the dynamic amplification $R = 1 + 0.06 \ln(\dot{\varepsilon})$ according to the calibrated Johnson-Cook model, while the right-hand-side of the same figure reports the percentage of area reduction as the time progresses, according to the Noble's experiments and to the FE simulations by Mirone (2013).

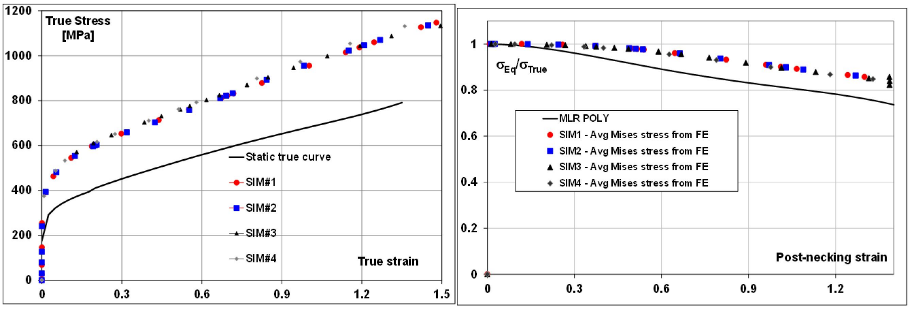

FIGURE 3. von Mises and True stresses (left), von Mises stress/True stress ratio and MLR function (right)

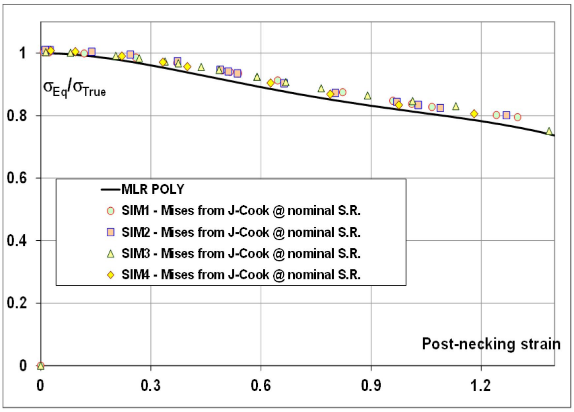

FIGURE 4. Flow stress/True stress ratio based on the true strain and the engineering strain rate.

Figure 2 shows, on the left-hand-side, the incident waves imposed along the input bar and, on the right-hand-side, the obtained evolution of the strain rate versus strain function using the engineering $(\varepsilon_{Eng}, \dot{\varepsilon}_{Eng})$ and the true approach $(\varepsilon_{True}, \dot{\varepsilon}_{True})$.

As it is possible to see on the left-hand-side of Figure 3, the obtained dynamic true curves at different strain rates are almost identical and significantly higher than the static one despite the used amplification law, depicted on the left-hand-side of Figure 1, is monotonically increasing also at large strain rates. Moreover, as it is possible to see on the right-hand-side of Figure 3, the postnecking ratio, $\sigma_{Eq}/\sigma_{True}$, diverged from the MLR prediction, already verified to be suitable for quasistatic cases (Mirone 2004).

According to the usual definitions, the engineering variables are based on load-elongation measurements and only apply up to early plastic stages, while the true variables are based on load-cross section measurements and are valid up to late postnecking stages and failure initiation:

$$\varepsilon_{Eng} = \frac{L - L_0}{L_0}, \qquad \sigma_{Eng} = F/A_0, \tag{2a}$$

TABLE 2. *Experimental plan for the FEN Steel*

L/d [-]	Specimen [-]	Diameter [mm]	Gage length [mm]	Bar preload [kN]	Nominal S.R. [s^{-1}]
≈ 1.0	FEN-S-D-11	2.9	3.0	15	750
≈ 1.0	FEN-S-D-12	3.0	3.5	18	1100
≈ 2.5	FEN-S-D-01	3.2	7.0	52	2800
≈ 2.5	FEN-S-D-02	3.1	7.6	50	2400
≈ 2.5	FEN-S-D-03	3.1	7.4	35	1600
≈ 2.5	FEN-S-D-04	3.1	7.5	38	1800
≈ 2.5	FEN-S-D-05	2.6	7.4	20	700
≈ 2.5	FEN-S-D-06	2.8	7.5	20	700
≈ 2.5	FEN-S-D-07	2.9	6.7	67	3600
≈ 2.5	FEN-S-D-08	2.9	6.7	71	3700
≈ 2.5	FEN-S-S-01	3.1	7.9	0	STATIC
≈ 2.5	FEN-S-S-02	3.1	7.6	0	STATIC
≈ 2.5	FEN-S-S-03	3.1	8.1	0	STATIC
≈ 2.5	FEN-S-S-04	3.0	8.2	0	STATIC
≈ 5.0	FEN-S-D-09	3.0	14.7	34	350
≈ 5.0	FEN-S-D-10	3.1	15.0	28	450

$$\varepsilon_{True} = \ln(A_0/A), \qquad \sigma_{True} = F/A, \tag{2b}$$

where the subscript "0" refers to the initial area and gage length of the undeformed specimens.

As far as smooth round specimens do not undergo necking, the stress state is uniform and uniaxial so that $\sigma_{vonMises} = \sigma_{True} =$ axial stress; beyond the necking onset, distributions of radial and hoop stresses develop in the neck zone, so the stress state is neither uniform nor uniaxial anymore: Then, $\sigma_{vonMises} \leq \sigma_{True}$ and only approximate models (e.g. Bridgman, MLR) are available for estimating the von Mises stress from true stress measurements.

Mirone (2013) also found, without a satisfactory explanation, that if σ_{Eq} for the ratio $\sigma_{Eq}/\sigma_{True}$ was calculated trough the Johnson-Cook function by using ε_{True} and $\dot{\varepsilon}_{Eng}$ from the FE results, then such ratio fully agreed with the MLR postnecking (Figure 4). Such outcomes needed further investigations and an explanation is discussed ahead in this paper.

3. SHTB experiments with FE360 mild steel

To further investigate such phenomena, an experimental-numerical campaign performed by the authors on a mild steel FE360, identified as FEN steel, partially shown by Mirone *et al.* (2016, 2017) is discussed below. The considered specimens are shown in Table 2 and Figure 5, in which there is also an example of an image acquired by the high frame rate camera used in the SHTB tests.

Figure 5 also shows an overview of the SHTB equipment available at the University of Catania. On the left-hand-side of Figure 6, the incident and the transmitted load waves of the SHTB FEN tests, slightly shifted for better readability, are shown. The corresponding curves

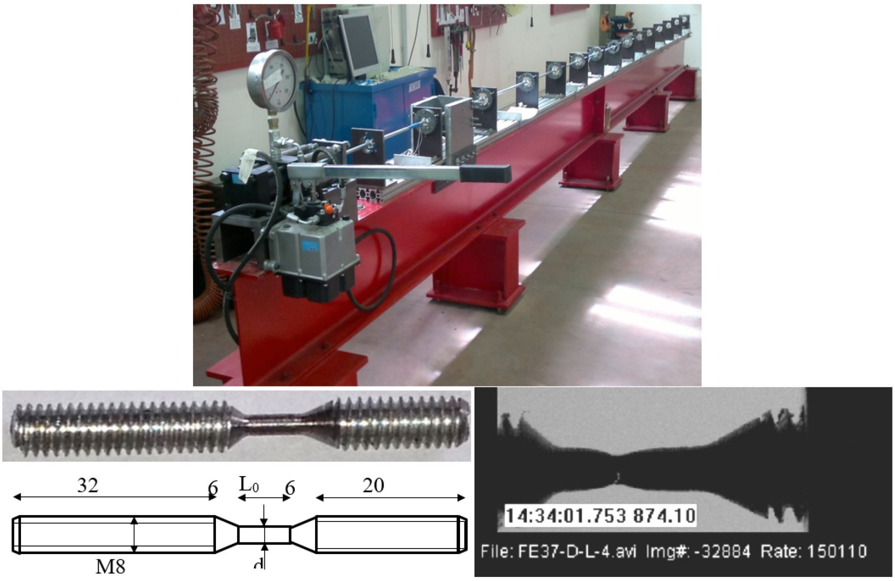

FIGURE 5. SHTB equipment and FEN specimens

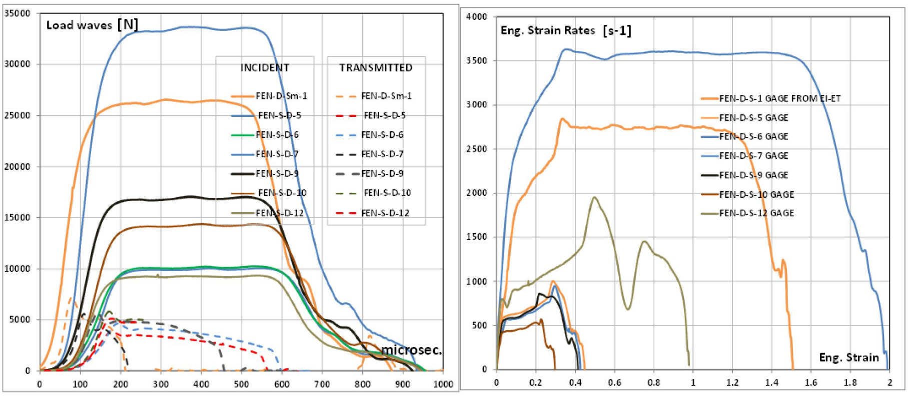

FIGURE 6. Elastic load waves along the bars (solid = incident, dashed= transmitted) (left); Engineering strain rates vs. Engineering strain (right)

relating the engineering strain rates (spanning from 450 to 3500 s-1) to the engineering strains are reported on the right-hand-side.

In Figure 7, the $\dot{\varepsilon}_{True}$ vs. ε_{True} and σ_{True} vs. ε_{True} curves from quasistatic and dynamic tests are shown. The necking initiation strain, ε_N, results to be independent of the strain rate and equal to 0.025. For comparison, the Remco iron showed an ε_N equal to 0.2.

Also in this case, as for the Remco iron and other experimental data from literature, despite very different strain rates tests (three-fold range of $\dot{\varepsilon}_{True}$), all the dynamic true

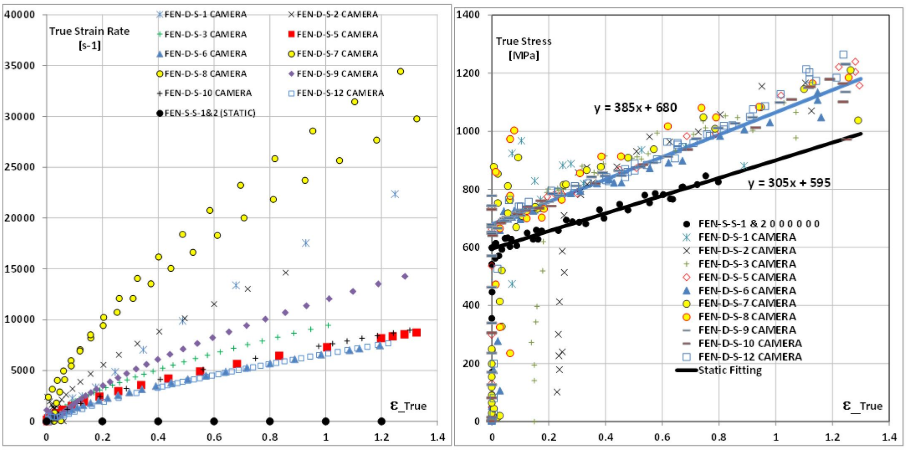

FIGURE 7. Experimental data from FEN steel, true strain rates (left), true curves (right)

curves appear to be confined in a rather narrow band, due realistically more to experimental scattering than strain rate effect, significantly higher than the static curve (right-hand-side of Figure 7). The true curves from the tests FEN-D-S 2 and 3 needed an offset of about 0.2 because of accidental prestrain generated during the machining as found by Rotbaum *et al.* (2015).

In the literature, this kind of behaviour is usually attributed to a strain rate effect that saturates very quickly at a strain rate in between the quasistatic test and the slowest dynamic test, which complies to the most known dynamic models like those by Johnson-Cook, Zerilli-Armstrong, Cowper-Symonds, etc. In the following, a new possible phenomenological explanation is discussed, regarding the interaction between the necking onset and the strain rate effect.

4. Material modeling of the FE360 mild steel and FE validation

For the characterization of the FEN steel, a general function including the uncoupled effects of the strain, of the strain rate and of the temperature is considered as in Equation (3). The σ_{Eq} is obtained by multiplying three terms representing respectively the quasistatic flow stress at room temperature, the dynamic amplification of the equivalent stress at room temperature, and the thermal softening:

$$\sigma_{Eq}\left(\varepsilon_{Eq},\dot{\varepsilon}_{Eq},T\right)=\sigma_{Eq\_S}\left(\varepsilon_{Eq},T_{\text{room}}\right)\cdot R(\dot{\varepsilon}_{Eq},T_{\text{room}})S(T). \qquad (3)$$

It is well known that, also in the postnecking phase, the differences between $\varepsilon_{Eq},\dot{\varepsilon}_{Eq}$ and $\varepsilon_{True},\dot{\varepsilon}_{True}$ are negligible. So, from now on, it is assumed that $\varepsilon_{Eq}\approx\varepsilon_{True}$ and $\dot{\varepsilon}_{Eq}\approx\dot{\varepsilon}_{True}$.

Considering the almost identical true curves obtained from the experiments, the plastic work adiabatically converted to heat in such experiments is almost equal, so $S(T)$ evolved in the same way for all the tests performed. Moreover, considering a realistic Taylor-Quinney coefficient smaller than unity, with simple calculation it is possible to verify that $S(T)$ is negligible at least until $\varepsilon_{True}\approx 0.3$, which, for the tests at hand, corresponds to $\dot{\varepsilon}_{True}$

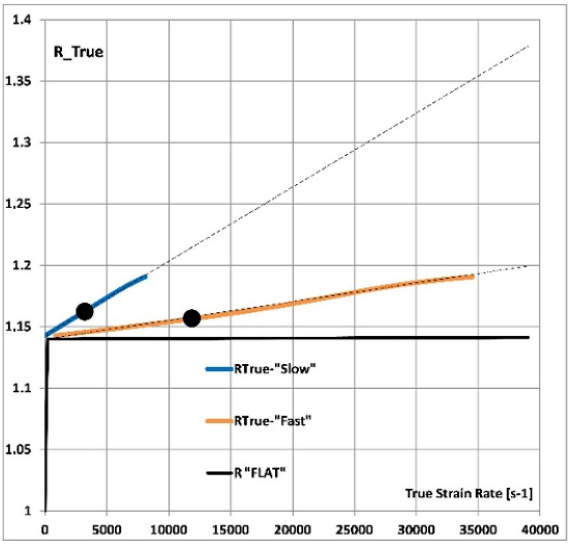

FIGURE 8. Possible dynamic amplification functions of the true stress for the FEN steel

values of 3000 s^{-1} (slower test) and 12000 s^{-1} (faster test). Only with plastic strains in excess of 0.6 ($\dot{\varepsilon}_{True} > 5000$ s^{-1} or $\dot{\varepsilon}_{True} > 20000$ s^{-1}), a temperature increment of 100 K can be reached and, after that, there could be an engineering detectable thermal softening. At incipient failure, the expected temperature increase of 250 K can generate significant softening effects. Then, the dynamic true amplification can be calculated just like the ratio between the dynamic and the static true curves obtained from the experiments, omitting the thermal effect also because the σ_{True} obtained from the dynamic test already includes the unknown thermal effect.

The two upper curves of Figure 8 are the R_{True} amplifications obtained from the fastest and the slowest dynamic tests. They should be almost the same being a material property but, excluded an initial very steep common part, from a strain just greater than the yield strain they differ greatly from each other depending on the different bar preloads. Tests with intermediate strain rates gave R_{True} curves in between the two. The filled circles depict the test stages where $\varepsilon_{True} = 0.3$, up to which the thermal softening is negligible.

Therefore, it seems that a very early event slightly after the first yield, very likely the necking onset (for the FEN steel $\varepsilon_N \approx 0.025$), triggers the path change between the curves, that were almost identical until then. Therefore, only until the necking onset the R_{True} versus the strain rate can be considered a material property. With the ε_N very close to zero, like in the FEN steel, it is necessary to have nearly rectangular incident waves to obtain significant differences in the nominal strain rate before necking. If we plot such amplifications versus the strain instead of the strain rate, we would obviously obtain the same curve (considering that the true curves obtained for all the tests are the same).

Since the amplification of the equivalent curve is not known in advance, the two amplification functions $R_{True\text{-}Fast}$ and $R_{True\text{-}Slow}$ are used as the most reasonable approximation of

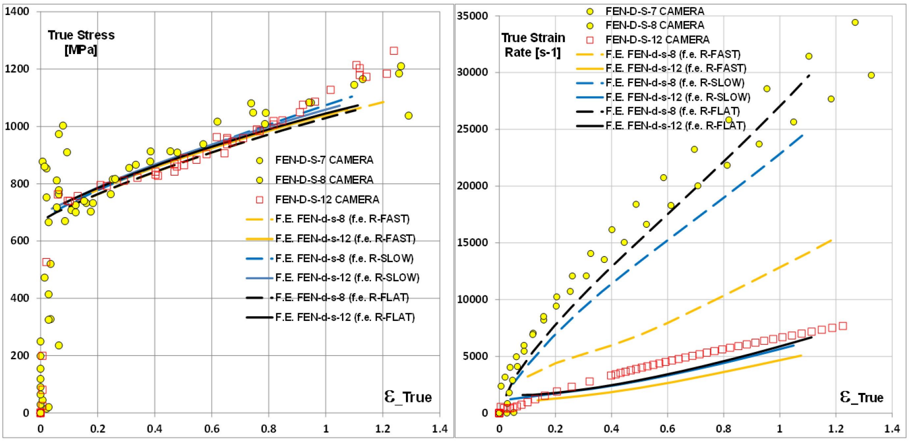

FIGURE 9. Numerical vs. experimental comparison of true curves (left) and true strain rates (right)

R_{Fast} and R_{Slow} of the equivalent curve to simulate the dynamic experiments. Moreover, a third equivalent amplification function R_{Flat} is considered here: it has the same common initial part as the others, but then it remains constant at the value of amplification occurring at the necking onset afterwards.

5. FE analysis of experiments and validation of the hardening model

Six simulations were run in total: Those of the slowest and of the fastest experiments, each one with the three different equivalent amplifications R_{Fast}, R_{Slow} and R_{Flat}. The FE models reproduce the complete SHTB system including elastic input and output bars; the axisymmetric mesh is rather large for the bars as only small elastic strains occur, while it is much finer for the elastoplastic specimen, with 18 elements along the specimen radius and smallest elements of about $0.04\,\text{mm} \times 0.075\,\text{mm}$.

The incident wave is imposed as a time-dependent pressure boundary condition applied to the free end of the input bar and it is left to propagate along the same bar until loading the specimen and being transmitted/reflected.

Updated Lagrangian formulation with additive decomposition of the strain is adopted for the large displacements-finite strain plasticity dynamics transient analysis. The isotropic hardening with von Mises yield surface and normality rule is selected within the MSC-MARC commercial code. The hardening function is implemented by the built-in Johnson-Cook material model for the standard JC simulations and by homemade user subroutines for the customized material models detailed below. The true curves obtained from the above simulations are plotted together with the corresponding experimental ones in the left part of the Figure 9. Analyzing the above figure, the simulated true curves are almost indiscernible from each other, despite having very different amplifications after the necking onset, and slightly underestimate the experimental true curve beyond of strains of 0.8.

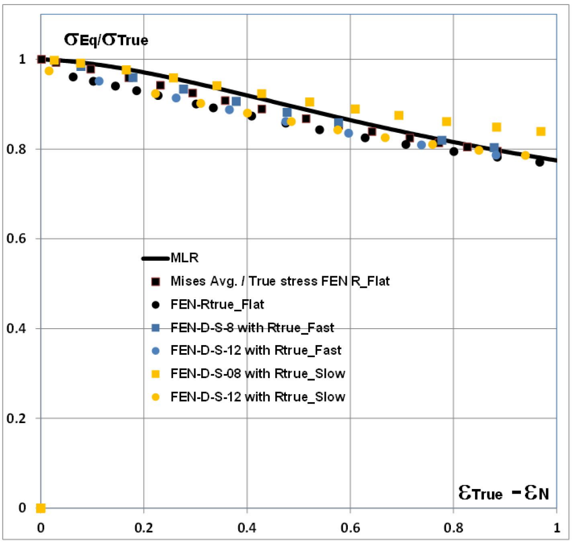

FIGURE 10. Dynamic true stress/flow ratio for the FEN steel

This means that only the amplification before the necking onset, common to all the simulations, is crucial for the complete test and that the successive part of the R functions has no effect on the actual evolution of σ_{True}. Therefore, the FE simulations are showing the same finding already shown by the experiments, and this means that this phenomenon is intrinsic in the equations of plasticity. As a first practical outcome, the true curve obtained from the experiments cannot be directly used to obtain the material dynamic amplification after the necking onset and it is not possible to use it for FE based reverse engineering in order to obtain the dynamic hardening amplification.

The problem of the identification of the dynamic amplification can be solved only using the $\dot{\varepsilon}_{True}$ histories. In fact, as it can be seen in the right part of Figure 9, only the R_{Flat} amplification allows to almost exactly reproduce such histories, thus confirming that the actual amplification due to the strain rate only acts until the necking onset and then it remains frozen to the current value.

As it is depicted in Figure 10, if the frozen amplification is correctly modeled, then the ratio between the dynamic equivalent stress and the dynamic true stress complies with the MLR function, confirming that the latter can also be used in the dynamic case.

Such results also imply that also the bars must be model together with the specimen for simulations of a SHTB test; also, the incident wave must be used as the boundary condition; in fact, the evolving $\dot{\varepsilon}_{True}$ is the result of the impedence-driven interaction between the bars and the specimen. In fact, if the experimental displacements are imposed to the specimen's ends, as frequently found in the literature, then hardening validation via comparison of experimental and FE strain rates becomes trivial, unless other iteration cross-controls are introduced like in (Peroni *et al.* 2015).

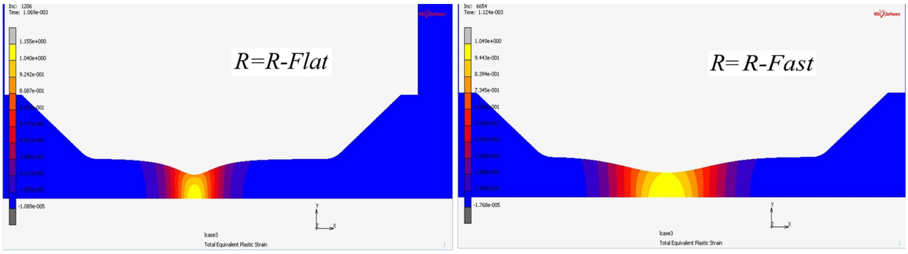

FIGURE 11. Effect of the dynamic amplification on the post-necking specimen shape

6. Outcomes of the interaction between necking and strain rate

Considering that the necking phenomenon is mainly a geometric effect, it is very likely that the flow amplification influences the shape of the specimen during the test. To check such effect, the shapes of the specimen at the same strain $\varepsilon_{True} = 1$ for two simulations of the FEN steel dynamic test, one with correct $R = R_{Flat}$ and the other with a spoiled $R = R_{Fast}$ are compared in Figure 11. As it is possible to see in such figure, with $R = R_{Fast}$, there is a more diffuse necking which is characterized by a lower triaxiality and, as a consequence, less difference between σ_{Eq} and σ_{True}. This phenomenon is well taken into account by Peroni *et al.* (2015), who proposed a reverse engineering technique in which the full profile of the specimen is considered in the iterative process.

The phenomenon of the interaction between necking and strain rate effect causes significant difficulties in the dynamic characterization of materials, especially those with very low necking strains. In fact, for such materials, only very low rise times of the incident wave allow to reach the high target values of the strain rate within the necking onset, which is the only way to perform the dynamic characterization with reference to the desired strain rate target. Such low rise times could be beyond feasibility or induce equilibrium and dispersion problems with the current techniques.

The rise time t_R of the incident wave is comparable to the one of the reflected wave, approximated as a trapezoid. Considering the classical SHTB theory, also the engineering strain rate is a linear function of the time within t_R with a slope α also depending on the speed of sound and on the specimen length:

$$\dot{\varepsilon}_{Eng}(t) = \alpha t, \qquad \varepsilon_{Eng}(t) = \alpha \frac{t^2}{2}. \tag{4}$$

Considering the target engineering strain rate, nominally constant, as the plateau of the reflected wave just after the rise time $\dot{\varepsilon}_{Eng}(t_R)$, the occurrence of the freezing effect implies that such target value must be reached before the necking onset, for it really affecting the material response. Therefore, the limit condition is when the necking onset occurs exactly at the end of the rise time:

$$\varepsilon_{Eng}(t_R) = \alpha \frac{t_R^2}{2} \quad \Rightarrow \quad \alpha = 2 \frac{\varepsilon_N}{t_R^2}. \tag{5}$$

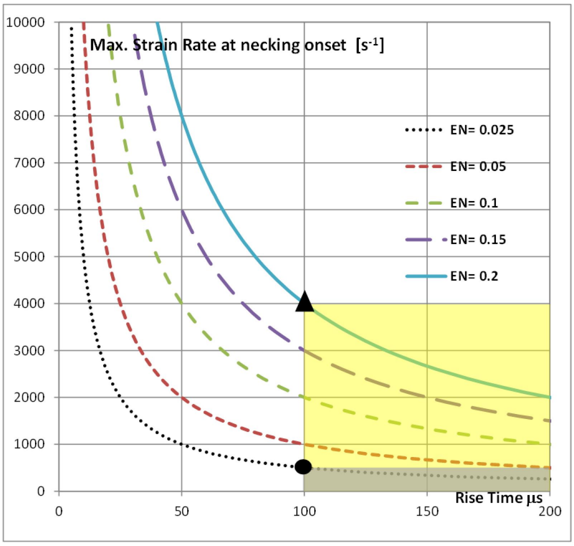

FIGURE 12. Maximum strain rate at the necking onset for given rise time and necking strain

Then, it is easy to calculate the limit strain rate $\dot{\varepsilon}_{Eng\text{-}L}$ to which the material is still responsive

$$\dot{\varepsilon}_{Eng\text{-}L} = \dot{\varepsilon}_{Eng}(t_R) = \alpha\, t_R = 2\frac{\varepsilon_N}{t_R}. \tag{6}$$

In Figure 12, as an example, such limit strain rate is plotted against the rise time for different values of the necking initiation strain.

Considering an SHTB setup characterized by a 100 microseconds rise time, the strain rate sensitivity of the FEN steel ($\varepsilon_N = 0.025$) might be tested up to about 500 s^{-1}, while the Remco iron ($\varepsilon_N \approx 0.2$) up to 4000 s^{-1}. In order to evaluate the strain rate sensitivity of the FEN steel at 5000 s^{-1} it would be necessary a rise time below 10 microseconds that is unrealistic with current SHTB setups.

Higher strain rates occurring on the specimens beyond the necking onset could not affect in any way the material response.

Further future investigations about the freezing of the strain rate effect might be useful for example including jump tests where the jump is performed before and after the necking initiation.

7. Conclusions

In this work, the interaction between the necking onset and the strain rate effect in SHTB tests has been studied by means of two experimental campaigns, the first published by Noble *et al.* (1999) and the second performed by the authors, both locally analysed via FE simulations.

The first important finding is that the strain rate effect on the σ_{True} is frozen at the necking onset both in the experiments and in the simulations, whichever dynamic hardening is implemented. Also the Johnson-Cook hardening model predicts that the dynamic amplification quits increasing as it gradually saturates. The main difference is that in the JC model the saturation is attributed to the achievement of large strain rates while in the present paper the freezing effect is attributed to the achievement of the strain at which the necking initiates.

Moreover, the dynamic amplifications of the true curves, obtained from the experiments and plotted versus the true strain rate, are the same in the pre-necking phase, while they greatly differ from each other afterwards, suggesting that such amplification can be considered a material property only in the first phase. If the stress amplification is plotted versus the strain, with the plateau strain rate as a curve parameter, then the independency of such amplification from the strain rate in the postnecking range becomes self-evident.

Then, it is found that the only amplification R of σ_{Eq} allowing FE to correctly reproduce the strain rate evolution of the tests is a law equal to all the R_{True} before the necking onset and constant at its last value afterwards. Using such correct equivalent amplification in FE, and successively plotting the ratio between the equivalent dynamic curve and the true dynamic curve obtained from the same FE output, it is possible to verify that the MLR function works, confirming that it can be used also in the dynamic case.

All these considerations confirm the importance of performing fast camera assisted tests in order to have the possibility of measuring the necking diameter.

What was found implies that the real effect of a certain $\dot{\varepsilon}_{True}$ can be observed if only it is achieved before the necking onset. Therefore, materials with very low necking strain, such as the FEN steel of this work, are very difficult to be properly characterized because they would need SHTB setups with too low rise times.

Future experiments with materials characterized by a high necking strain and SHTB setups with a controllable rise time could help to better understand further details of this phenomena and the in-depth reasons why it occurs.

In Memoriam

Professor Gaetano Giaquinta was a free transparent personality before being an esteemed rigorous scientist. He professed the exercise of curiosity without preconceptions and of honesty without shortcuts, together with physics and, sometimes, with a little bit of philosophycal aspects of physics too. Would you believe that such a man was also blessed with an extremely fine sense of humor? Well he was. And one of his lessons I still remember with more pleasure included cats diagonalizing their intertia matrix while jumping from the balcony on the 3rd floor .... Professor Giaquinta, see you.

References

Besnard, G., Hild, F., Lagrange, J.-M., Martinuzzi, P., and Roux, S. (2012). “Analysis of necking in high speed experiments by stereocorrelation”. *International Journal of Impact Engineering* **49**, 179–191. DOI: 10.1016/j.ijimpeng.2012.03.005.

Bridgman, P. W. (1952). *Studies in Large Plastic Flow and Fracture*. New York-London: McGraw-Hill.

Mirone, G., Corallo, D., and Barbagallo, R. (2016). “Interaction of strain rate and necking on the stress-strain response of uniaxial tension tests by Hopkinson bar”. *Procedia Structural Integrity* **2**, 974–985. DOI: 10.1016/j.prostr.2016.06.125.

Mirone, G., Corallo, D., and Barbagallo, R. (2017). “Experimental issues in tensile Hopkinson bar testing and a model of dynamic hardening”. *International Journal of Impact Engineering* **103**, 180–194. DOI: 10.1016/j.ijimpeng.2017.01.005.

Mirone, G. (2004). “A new model for the elastoplastic characterization and the stress–strain determination on the necking section of a tensile specimen”. *International Journal of Solids and Structures* **41**(13), 3545–3564. DOI: 10.1016/j.ijsolstr.2004.02.011.

Mirone, G. (2013). “The dynamic effect of necking in Hopkinson bar tension tests”. *Mechanics of Materials* **58**, 84–96. DOI: 10.1016/j.mechmat.2012.11.006.

Noble, J., Goldthorpe, B., Church, P., and Harding, J. (1999). “The use of the Hopkinson bar to validate constitutive relations at high rates of strain”. *Journal of the Mechanics and Physics of Solids* **47**(5), 1187–1206. DOI: 10.1016/s0022-5096(97)00090-2.

Peirs, J., Verleysen, P., Paepegem, W. V., and Degrieck, J. (2011). “Determining the stress–strain behaviour at large strains from high strain rate tensile and shear experiments”. *International Journal of Impact Engineering* **38**(5), 406–415. DOI: 10.1016/j.ijimpeng.2011.01.004.

Peroni, L., Scapin, M., and Fichera, C. (2015). “An advanced identification procedure for material model parameters based on image analysis”. In: *10th European LS-DYNA Conference tenutosi a Würzburg (Germania)*.

Rotbaum, Y., Osovski, S., and Rittel, D. (2015). “Why does necking ignore notches in dynamic tension?” *Journal of the Mechanics and Physics of Solids* **78**, 173–185. DOI: 10.1016/j.jmps.2015.02.005.

Rusinek, A., Zaera, R., Klepaczko, J., and Cheriguene, R. (2005). “Analysis of inertia and scale effects on dynamic neck formation during tension of sheet steel”. *Acta Materialia*. DOI: 10.1016/j.actamat.2005.08.019.

Sato, K., Yu, Q., Hiramoto, J., Urabe, T., and Yoshitake, A. (2015). “A method to investigate strain rate effects on necking and fracture behaviors of advanced high-strength steels using digital imaging strain analysis”. *International Journal of Impact Engineering* **75**, 11–26. DOI: 10.1016/j.ijimpeng.2014.07.001.

---

[a] Università degli Studi di Catania,
Dipartimento di Ingegneria Civile e Architettura,
Viale Andrea Doria 6, 95125 Catania, Italy

* To whom correspondence should be addressed | email: gmirone@dii.unict.it

Manuscript received 10 April 2017; published online 13 August 2018